Self-healing of the statistical properties of exact non-Rayleigh nondiffracting speckle fields

José G. M. N. Neto ⊕,* Izaque J. S. Melo ⊕, Eduardo J. S. Fonseca, and Alcenísio J. Jesus-Silva ⊕†

Optics and Nanoscopy Group, Institute of Physics, Federal University of Alagoas, Maceió, Alagoas 57072-900, Brazil

We investigate the capacity of the exact non-Rayleigh nondiffracting (ENRND) speckle field to reconstruct its statistical properties along the propagation. It is unclear in the literature how the statistical properties of such a speckle field can affect the reconstruction of the statistics itself after encountering an obstruction. Therefore, we have conducted this study using the first-order and second-order intensity statistics, revealing a remarkable superior robustness of the super-Rayleigh speckles. This study has the potential to be beneficial for future applications of speckles with controlled statistics in microscopic systems and quantum imaging.

The light of a coherent laser scattered from rough objects results in a kind of light with a peculiar granular appearance, known as speckle light. This type of light is an interference between many independent partial waves with relative phases uniformly distributed in the range of 2π. Typically, the amplitude of the speckle fields present a Rayleigh probability density function (PDF) and the speckles intensity follows a negative exponential PDF [1]. On the other hand, the self-healing, or the capacity of reconstruction of the intensity pattern, was observed first in Bessel beams [2–4], followed by Airy beams [5–7] and even Laguerre-Gaussian beams [8]. A similar effect was observed for diffracting Rayleigh speckles [9], but it was called self-reconfiguration because the speckle patterns are not the same after the reconstruction. True self-healing is observed only for nondiffracting speckles [10]. The self-healing and self-reconfiguration abilities can be applied in microscopy [2,3], quantum optics communication [11,12], and three-dimensional imaging processes through an inhomogeneous medium [13].

The non-Rayleigh speckle statics regime occurs when the spatial structure of the speckle intensity pattern is customized without losing the random granular structure of light. The non-Rayleigh speckle can be generated using a spatial light modulator (SLM) to codify high-order correlation in the front phase of an input field [14–19]. The non-Rayleigh speckles can be nondiffracting [18] and even diffracting and maintaining the non-Rayleigh statistical properties through the distance of propagation [20]. The non-Rayleigh speckles also have found applications in microscope systems [21] and for ghost imaging [22,23]. Therefore, studies on the robustness of the statistics, similar to the robustness of the speckle itself [9], in the context of exact non-Rayleigh nondiffracting (ENRND) speckle fields [19], can prove useful for systems that demand controllable visibility [24]. These applications can be found in optical encryption and optical tomography.

For Bessel beams, the beam parameter that governs the reconstruction distance is solely the transverse spatial frequency

[9]. However, for the self-reconfiguration of speckle fields, it relies on the spatial coherence length [25]. But, it is not clear how the statistics affect this reconstruction length, therefore in the present study we examine the impact of first-order and second-order intensity statistics on the distance required for reconstructing these statistical properties in the generated non-Rayleigh speckle fields. Additionally, we propose a more efficient and faster method for generating ENRND speckle fields, improving the method described in Ref. [19]. As a result, we will be able to generate multiple samples of intensity patterns with contrast values ranging from sub-Rayleigh to super-Rayleigh statistics. This will enable us to analyze the behavior of the first- and second-order intensity statistics of an ENRND speckle field since this investigation requires averaging over a set of random realizations of the pattern.

Our objective is to write the discrete form of the Whittaker integral [19] as a Fourier transform of a ring-shaped function $S(k_x, k_y)$,

$$U(x, y) \propto \int S(k_x, k_y) e^{-i\mathbf{k}_T \cdot \mathbf{r}_T} d\mathbf{k}_T, \tag{1}$$

so that we represent the $S(k_x, k_y)$ as

$$S(k_x, k_y) = \sum_n \Phi(\phi_n)\delta(k_x - k_T \cos\phi_n, k_y - k_T \sin\phi_n), \tag{2}$$

where $\phi_n = 2n\pi/(Q - 1)$, $n = 0, \ldots, Q - 1$ and $\Phi(\phi_n) = \exp[i\theta(\phi_n)]$. We have used the same optimization algorithm as in Ref. [19]. Therefore, we have considered that the phase array θ is the sum of two random arrays A and B, whose entries are uniformly distributed over $[0, 2\pi]$. In this case, $\theta = A + B$, both with length $Q = 1024$. The necessity of summing B to A is just to generate a uniformly distributed random array $A + B$, but with some correlations, in order to control the speckles statistics. It is an artifact of this procedure that if you do not add the constant array B to the optimized array A the algorithm converges to a coherent pattern. The uniformly distributed random numbers used for optimizing the array A are taken from a phase array D with $N = 150$ random values, which is the minimum number of values to guarantee convergence. As displayed in Fig. 1, we replaced one fixed position of A with the values of D, and calculated
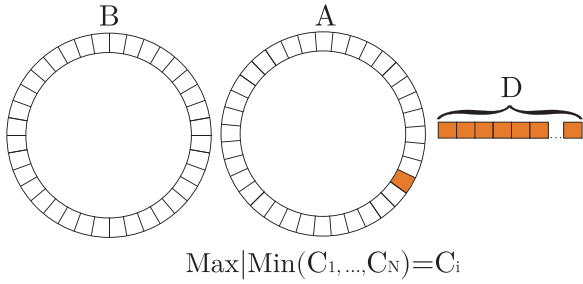
*josé.gilson@fis.ufal.br
†alcenisio@fis.ufal.br

FIG. 1. Representation of the positions of the pixels corresponding the phase values in the ring-shaped function in Eq. (2). During each iteration, the contrast value is optimized to each position "i" of A that is randomly chosen at the beginning of the iteration. This position remains fixed throughout the iteration process.

the sum in Eq. (1) for the N possible values and chose the one that gives the best contrast. It corresponds to one iteration of the algorithm. After each iteration the random values of D are updated. If we desire a super-Rayleigh speckle field we select A that have the biggest contrast, and if we want a sub-Rayleigh speckle we choose A that have the smallest contrast.

The novelty of the optimization algorithm lies in the fact that the speckle field represented in Eq. (1) is just a Fourier transform and not a time-consuming plane wave summation. We utilize the concept that the spatial Fourier spectra of a nondiffracting beam can be represented as a ring with infinitesimal width and radius k_T. By doing so, we express each plane wave in Eq. (1) as a single pixel within this ring, as illustrated in Fig. 1. This is elucidated by understanding that nondiffracting beams consist of a collection of plane waves characterized by wave vectors situated on the surface of a light cone, all possessing identical amplitudes and equivalent longitudinal components of the wave vector k_z [26]. It can be written that $k_z = \sqrt{k^2 - k_T^2}$, where $k = 2\pi/\lambda$, $k_x = k_T \cos\phi$, $k_y = k_T \sin\phi$, and λ is the wavelength of the light [18]. Therefore, to perform our summation algorithm we defined a function to calculate the coordinates of the pixels along the ring by the pseudocode in Fig. 2.

In Fig. 3, we compare the intensity patterns of a speckle field plotted with the aid of the algorithm based on the Fourier transform, displayed in Fig. 3(a), and using the discrete form of the Whittaker integral [19], displayed in Fig. 3(b). The process of calculating the sum using the Fourier transform is 700 times faster. We can observe that the speckle patterns have

Algorithm 1 Assigning phase values to a ring of pixels

1: **procedure** $S(A, B, k_T, N, Q)$
2: **begin**
3: $S[N, N] = 0$;
4: **for** $n := 1$ **to** Q **do**
5: $\qquad k_x = \lfloor k_T \cos(2n\pi/Q) \rfloor + \lfloor N/2 + 1 \rfloor$;
6: $\qquad k_y = \lfloor k_T \sin(2n\pi/Q) \rfloor + \lfloor N/2 + 1 \rfloor$;
7: $\qquad S(k_x, k_y) = \exp\{i[A(n) + B(n)]\}$;
8: **end.**

FIG. 2. The pseudocode of the function used to calculate the position of the phase values in the ring-shaped function in Eq. (2). The symbol $\lfloor\ \rfloor$ stands for the nearest integer.
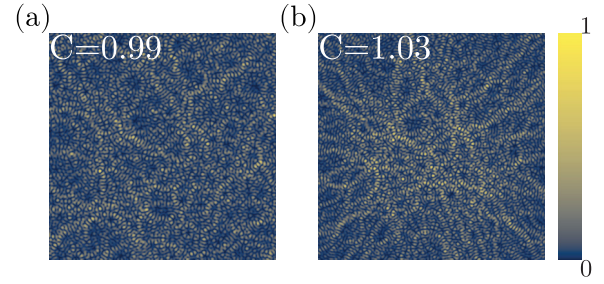

FIG. 3. Numeric intensity pattern for nondiffracting speckle fields in the Rayleigh regime. In (a), we utilized the Fourier transform to sum the plane waves following Eq. (1), and in (b), we summed the plane waves following Ref. [19].

the same contrast and the same medium speckle grain size, which are the important characteristics for the generated random patterns. Figure 4 shows our experimental setup. A laser model Ultralasers MSL-FN-532, of 200 mW and operating in 532 nm, uniformly illuminates a Holoeye LETO spatial light modulator (SLM), placed at the distance $d = 540$ mm from the lens L3, of focal length $f3 = 1000$ mm. In the focus of lens L3, we separated the first diffraction order using an iris (IR). We used a computer-generated phase hologram (CGPH) of type 3 [27], which is encoded in the SLM and contains the phase and amplitude of the calculated speckle field and a circular obstacle partially blocking the speckle field. The lens L4 has a focal length $f4 = 150$ mm, where L4 was confocal with the lens L3. Therefore, near the focus of the L4 we have the image of the SLM, the ENRND speckle field with
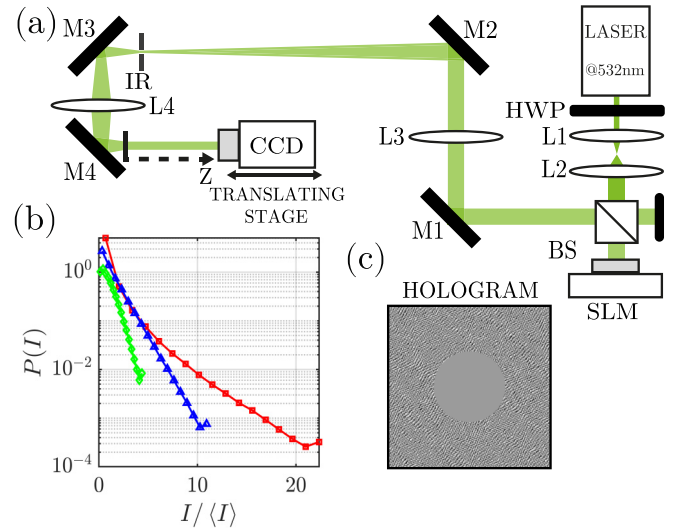

FIG. 4. (a) The experimental setup: HWP is a half-wave plate; L1, L2, L3, and L4 are lenses; BS is a beam splitter; SLM is the spatial light modulator; M1, M2, M3, and M4 are mirrors; A is a circular aperture; and CCD is a charge-coupled device camera. (b) Intensity histograms for the measured intensity patterns: the red squares, blue triangles, and green diamonds correspond to the super-Rayleigh, Rayleigh, and sub-Rayleigh speckles, respectively. Each of these intensity histograms was obtained by averaging over 100 measurements of random speckle intensity patterns. (c) A hologram featuring a circular obstacle.
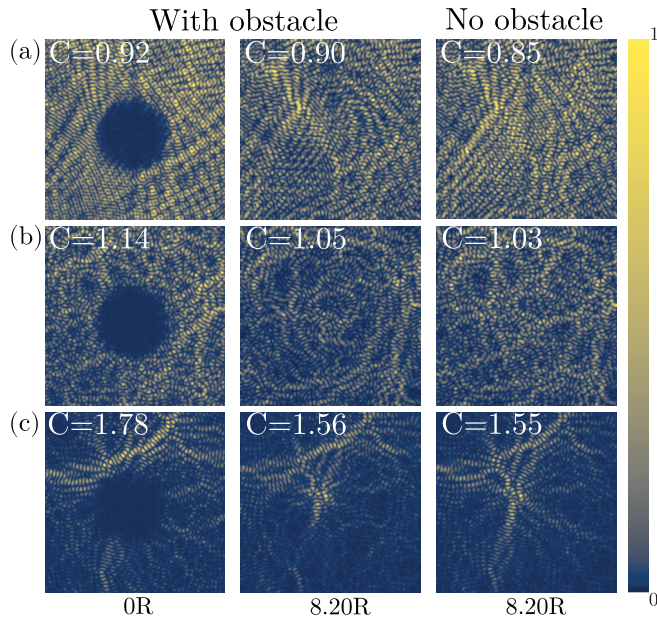
FIG. 5. Experimental self-healing effect for the ENRND speckle field. The intensity pattern for (a) sub-Rayleigh speckles, (b) Rayleigh speckles, and (c) super-Rayleigh speckles.

a circular obstacle in the center of the intensity pattern. A charge-coupled device (CCD) camera, which is mounted on a translating stage, was used for the experimental measurements of the speckle transverse profile reconstruction along the propagation. For each measurement, the ENRND speckle fields were propagated over 8.2 Rayleigh ranges, where the measurement of one Rayleigh range resulted in $R = 0.16$ mm.

To understand the physics behind the self-healing effect of the statistics in the ENRND speckle fields, we will compare the speckle's first-order and second-order intensity statistics [1]. The first-order statistics of the speckle intensity is related to the contrast, accounting for, in statistical properties, about a single point in the transverse plane with coordinates $\mathbf{x} = (x, y)$. We considered the following definition to the contrast:

$$C = \sqrt{\frac{\langle I(x)^2 \rangle}{\langle I(x)^2 \rangle} - 1},$$ (3)

where $I(\mathbf{x}) = |U(\mathbf{x})|^2$ is the intensity, the symbol $\langle \rangle$ indicates the mean, and this contrast definition is the ratio between the standard deviation and the mean intensity.

Figure 5 displays the self-healing effect for different statistical regimes: sub-Rayleigh, Rayleigh, and super-Rayleigh. All obstacles have a diameter of $d = 0.8$ mm and are positioned at the initial point of propagation ($z = 0R$). We have used a window of 1.3 mm × 1.3 mm of the CCD camera for all the results in this work. In the first column of Fig. 5 the patterns are partially blocked by the obstacle and are in the initial position of propagation ($z = 0R$). In Fig. 5(a) the ENRND speckle field is in the sub-Rayleigh regime. The speckle intensity pattern in the second column represents the reconstructed speckle patterns at 8.20R with a contrast $C = 0.90$. In the same line, third column, the same sub-Rayleigh speckle without obstacle at distance $z = 8.20R$ has the
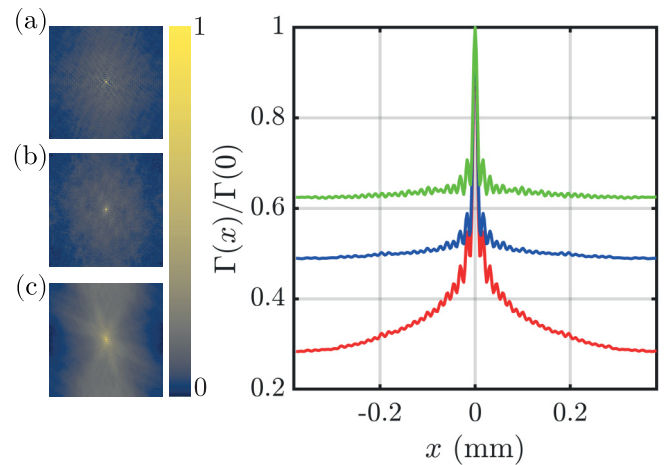

FIG. 6. Second-order spatial intensity correlations for the ENRND speckle field. (a) The intensity pattern for sub-Rayleigh speckles, (b) the Rayleigh speckles, and (c) the super-Rayleigh speckles.

contrast $C = 0.85$. At 0R the contrast for the sub-Rayleigh speckle without obstacle was $C = 0.78$; therefore, we observe an increase in the speckle contrast after inserting the obstacle. However, the spatial features and contrast of the reconstructed speckle field approach the values obtained with no obstacles. Similar behaviors were observed for the Rayleigh and super-Rayleigh fields at Figs. 5(b) and 5(c), respectively. In Fig. 5(b), we analyzed the self-healing behavior of the Rayleigh speckles. We observed that the contrast along the propagation path returns toward the value obtained for the speckles with no obstacles. Figure 5(c) shows the intensity pattern for speckles in the super-Rayleigh regime, where the intensity pattern reconstructed at the distance 8.20R has contrast $C = 1.56$ and the intensity pattern without obstacles has contrast $C = 1.55$. The contrast for the super-Rayleigh speckles with no obstacles at the initial position $z = 0R$ was $C = 1.66$, relatively closer to the final value at $z = 8.2R$. Its important to call attention to the sub-Rayleigh speckle fields, as both blocked and nonblocked speckles exhibit a trend towards Rayleigh statistics during propagation. This transition occurs due to the degradation of sub-Rayleigh speckle statistics along propagation, impeding a more pronounced reconstruction towards the contrast value of $C = 0.78$. Now, we will introduce the second-order statistics of the speckle intensity. To quantify these statistics, we will use the second-order spatial intensity correlations [28],

$$\Gamma(\mathbf{x}) = \left\langle \int_{\Omega} I(\mathbf{x}')I(\mathbf{x}' - \mathbf{x}) \, d\mathbf{x}' \right\rangle$$
$$= \int_{\Omega} \langle I(\mathbf{x}')I(\mathbf{x}' - \mathbf{x}) \rangle \, d\mathbf{x}',$$ (4)

where Ω indicates the domain of the integral. Using the procedure described in Eq. (4), we can calculate the normalized second-order speckle correlation function displayed in Fig. 6. These results are obtained averaging over 100 samples of speckles without any obstacles. The green, blue, and red line plots at the right of Fig. 6 correspond to the sub-Rayleigh, Rayleigh, and super-Rayleigh statistics, respectively. They are

horizontal profiles taken at the center of Figs. 6(a), 6(b), and 6(c), respectively. The smallest background is observed for the super-Rayleigh speckles. The noncorrelated speckle grains are responsible for the background [9], therefore the sub-Rayleigh speckles have a bigger number of noncorrelated speckle grains than the super-Rayleigh speckles. The number of noncorrelated speckle grains is not simply proportional to the area outside the coherence length divided by the coherence length. Regardless of the statistics, all speckle patterns have a coherence length of 0.01 mm, which is measured as the full width at half maximum of the correlation function, roughly the size of a speckle grain. However, the super-Rayleigh speckle patterns have less speckle grains in a given area because the light is concentrated in a fewer speckle grains and the grains are more spaced between each other. Therefore, the super-Rayleigh speckles have an increased spatial coherence even with the same coherence length as the sub-Rayleigh speckles. It also may be understood in terms of the spatial spectral density [29], which is the spatial distribution of the light along the spatial frequencies. The coherence information is not just in the coherence length but also in the spectral density. The spectral density contributes to the background but is not totally dependent on the coherence length. To understand the behavior of the second-order intensity statistics we calculate the visibility of the correlation function [30,31]

$$V = \frac{\Gamma_{\max} - \Gamma_{\min}}{\Gamma_{\max}}, \tag{5}$$

where $\Gamma_{\max}$ and $\Gamma_{\min}$ are the maximum and minimum values of the correlation function. Figure 7 compares the contrast and the visibility during the propagation for approximately 8.20 Rayleigh ranges. Each point in the curves of Fig. 7 is obtained averaging the results over 100 measured intensity patterns. Continuous lines represent the self-healing effect and the dashed lines represent the results without blocking the speckle fields. Red, blue, and green lines represent the super-Rayleigh, Rayleigh, and sub-Rayleigh regimes, respectively. In Fig. 7(a) we observe the behavior of the first-order intensity statistic, represented through the contrast. The contrast of the super-Rayleigh patterns after crossing the obstacle at the initial position $z = 0$R is $C = 1.66$, and at the final position at $z = 8.20$R it is $C = 1.53$. This result should be compared with results for the super-Rayleigh speckles without obstacles, at $z = 0$R, where $C = 1.56$, and at $z = 8.20$R, where $C = 1.50$. In other words, the super-Rayleigh regime almost recovers its first-order statistical properties after the self-healing effect. For the Rayleigh regime, represented in the blue lines, the self-healing effect is also observed. At $z = 0$R the value of the contrast is $C = 1.13$, after crossing the obstacle, and at $z = 8.20$R the contrast is $C = 1.09$, near the value for the Rayleigh speckles without obstacles. For the sub-Rayleigh regime, the green lines, after crossing the obstacle at $z = 0$R, the value of contrast is $C = 0.91$, and at $z = 8.20$R the value is $C = 0.89$, which without obstacles evolves from $C = 0.77$ to $C = 0.80$. Mainly in the sub-Rayleigh speckles we observe some degradation of the statistics, moving the contrast value in the direction of value $C = 1$ of the Rayleigh speckles. Therefore, to make these results clearer, we displayed in Fig. 7(c) the difference between the results for the speckle field that crossed an obstacle and the one that did not cross any
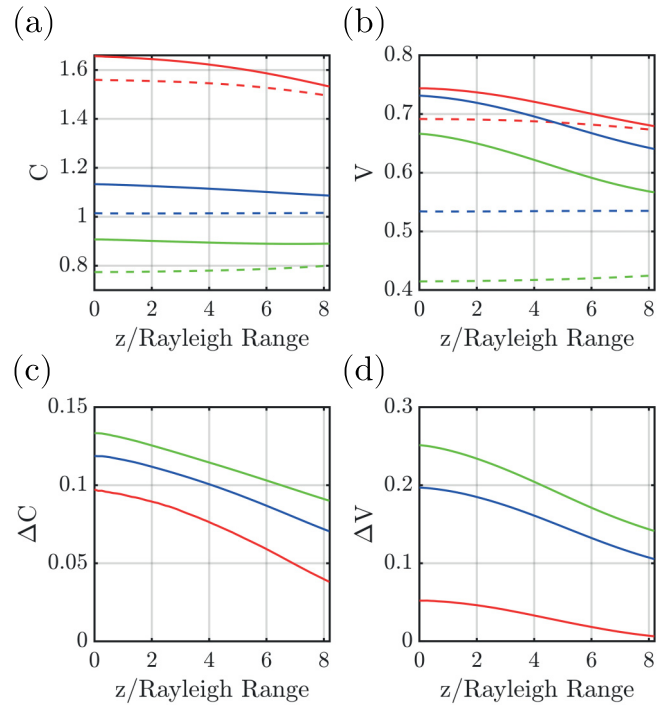

FIG. 7. Experimental results for the intensity statistics along different axial positions. (a and b) Behavior of the contrast and visibility, respectively, during the self-healing effect in the axial propagation of Rayleigh speckles (blue line), sub-Rayleigh speckles (green line), and super-Rayleigh speckles (red line). The dotted lines correspond to the results without obstacles. (c and d) The difference between the results with and without obstacles.

obstacle. We can conclude that this difference is decreasing with the propagation, indicating the amount of the self-healing effect of the contrast.

To understand the behavior of the second-order intensity statistics we analyzed the visibility of the correlation function in Fig. 7(b). The line colors and the use of dashed and continuous lines represent the same meaning as that used for the contrast. Therefore, the results for the second-order statistics agree with the results for the first-order statistics. When the intensity pattern is blocked, the visibility increases, and as the propagation continues, the self-healing effect takes place, recovering the statistical properties of the field. The difference between the intensity correlation visibility with and without obstacles, Fig. 7(d), decays during the propagation. It is worth emphasizing that upon analyzing the statistics of all speckle fields, we noted that the impact of the obstacle is least pronounced for super-Rayleigh speckles when compared to other statistical regimes. This finding could serve as a justification for choosing super-Rayleigh speckles in applications related to imaging and microscopy.

Following the ideas of Ref. [25], we have proposed a theoretical estimation for the reconstruction distance z_R. Suppose that a single speckle grain has a mean width equal to the coherence length δ and that it could be represented by $\exp(-r^2/2\delta^2)$, where r is the radial coordinate. Each speckle spot in the field that surrounds the opaque disk acts as a secondary source that radiates into the disks shadow, filling in the dark hole in the field due to the circular obstacle. The

distance for the total reconstruction of a Rayleigh speckle is obtained by equating the width of the central lobe of an Airy pattern, of a circular aperture having the same diameter d of the obstacle, with the full width at half maximum of the function $\exp(-r^2/2\delta^2)$. The effect of having a bigger or smaller background for other statistics could be estimated by adding a constant to the speckle grain function $\Delta b + \exp(-r^2/2\delta^2)$, therefore its full width at half maximum is shifted and we have

$$z_R = \frac{2\delta\sqrt{2}d}{1.22\lambda}\sqrt{\ln\frac{2}{1-2\Delta b}},$$

where $b = \Gamma_{\max} - \Gamma_{\min}$, and Δb is the difference in relation to the Rayleigh background. Using the data from the experiment, $\Delta b_{\text{sub-Rayleigh}} = 0.13$, $\Delta b_{\text{Rayleigh}} = 0$ and $\Delta b_{\text{super-Rayleigh}} = -0.23$, and therefore, $z_R = 34.8\,\text{mm}$, $z_R = 29\,\text{mm}$ and $z_R = 19.6\,\text{mm}$, for the sub-Rayleigh, Rayleigh, and super-Rayleigh speckles, respectively.

In summary, we analyzed the self-healing of the statistical properties of ENRND speckle fields. Besides, we proposed a faster method to calculate a sum of plane waves to form a nondiffractive field. This procedure generates an approximation to the exact solution of the Helmholtz equation. This method can generate a continuous range of contrast values in the sub-Rayleigh, Rayleigh, and super-Rayleigh regimes, preserving the nondiffractive property. Our results demonstrated that the super-Rayleigh regime had better reconstruction of contrast and visibility during the self-healing effect, demonstrating that these speckle fields can be used to improve the spatial resolution in the ghost image process with applications in optical encryption and optical tomography, or imaging through a scattering medium [13]. Similar effects should be observed in other types of non-Rayleigh speckles, such as three-dimensional speckles [20], in cases where they possess statistics that lead to an increased or decreased background in the intensity correlation.

[1] J. Goodman, *Speckle Phenomena in Optics: Theory and Applications* (Roberts & Company, Englewood, 2007).

[2] F. O. Fahrbach, P. Simon, and A. Rohrbach, Microscopy with self-reconstructing beams, Nat. Photon. **4**, 780 (2010).

[3] F. O. Fahrbach and A. Rohrbach, Propagation stability of self-reconstructing Bessel beams enables contrast-enhanced imaging in thick media, Nat. Commun. **3**, 632 (2012).

[4] J. Durnin, J. Miceli, Jr., and J. H. Eberly, Diffraction-free beams, Phys. Rev. Lett. **58**, 1499 (1987).

[5] X. Chu, G. Zhou, and R. Chen, Analytical study of the self-healing property of Airy beams, Phys. Rev. A **85**, 013815 (2012).

[6] L. Zhang, F. Ye, M. Cao, D. Wei, P. Zhang, H. Gao, and F. Li, Investigating the self-healing property of an optical Airy beam, Opt. Lett. **40**, 5066 (2015).

[7] Y. Zhao, Y. Wang, Q. Chen, P. Ma, Y. Cai, and C. Liang, Enhancing the self-healing ability of a partially coherent Airy beam via Fourier processing: Numerical investigation, in *Photonics* (MDPI, Basel, 2023), Vol. 10, p. 143.

[8] J. Mendoza-Hernández, M. L. Arroyo-Carrasco, M. D. Iturbe-Castillo, and S. Chávez-Cerda, Structured light beams constituted of incoming and outgoing waves, Phys. Rev. A **100**, 053847 (2019).

[9] C. R. Alves, A. J. Jesus-Silva, and E. J. Fonseca, Self-reconfiguration of a speckle pattern, Opt. Lett. **39**, 6320 (2014).

[10] D. M. Cottrell, J. M. Craven, and J. A. Davis, Nondiffracting random intensity patterns, Opt. Lett. **32**, 298 (2007).

[11] M. McLaren, T. Mhlanga, M. J. Padgett, F. S. Roux, and A. Forbes, Self-healing of quantum entanglement after an obstruction, Nat. Commun. **5**, 3248 (2014).

[12] X. Wang, J. Fu, S. Liu, Y. Wei, and J. Jing, Self-healing of multipartite entanglement in optical quantum networks, Optica **9**, 663 (2022).

[13] D. G. Pires, A. F. Sonsin, A. J. Jesus-Silva, and E. J. Fonseca, Three-dimensional speckle light self-healing-based imaging system, Sci. Rep. **8**, 563 (2018).

[14] Y. Bromberg and H. Cao, Generating non-Rayleigh speckles with tailored intensity statistics, Phys. Rev. Lett. **112**, 213904 (2014).

[15] J. P. Amaral, E. J. S. Fonseca, and A. J. Jesus-Silva, Tailoring speckles with Weibull intensity statistics, Phys. Rev. A **92**, 063851 (2015).

[16] N. Bender, H. Yılmaz, Y. Bromberg, and H. Cao, Customizing speckle intensity statistics, Optica **5**, 595 (2018).

[17] N. Bender, H. Yılmaz, Y. Bromberg, and H. Cao, Creating and controlling complex light, APL Photon. **4**, 110806 (2019).

[18] R. Liu, B. Qing, S. Zhao, P. Zhang, H. Gao, S. Chen, and F. Li, Generation of non-Rayleigh nondiffracting speckles, Phys. Rev. Lett. **127**, 180601 (2021).

[19] J. G. Neto, E. J. Fonseca, and A. J. Jesus-Silva, Exact solutions for non-Rayleigh nondiffracting speckles, Phys. Rev. A **106**, 053519 (2022).

[20] S. Han, N. Bender, and H. Cao, Tailoring 3D speckle statistics, Phys. Rev. Lett. **130**, 093802 (2023).

[21] N. Bender, M. Sun, H. Yılmaz, J. Bewersdorf, and H. Cao, Circumventing the optical diffraction limit with customized speckles, Optica **8**, 122 (2021).

[22] K. Kuplicki and K. W. C. Chan, High-order ghost imaging using non-Rayleigh speckle sources, Opt. Express **24**, 26766 (2016).

[23] E.-F. Zhang, W.-T. Liu, and P.-X. Chen, Ghost imaging with non-negative exponential speckle patterns, J. Opt. **17**, 085602 (2015).

[24] D. Zhou, L. Zhang, H. Zhang, and G. Zhang, Ghost images with controllable visibility and spatial resolution, Opt. Express **31**, 14659 (2023).

[25] C. R. Alves, A. J. Jesus-Silva, and E. J. S. Fonseca, Effect of the spatial coherence length on the self-reconfiguration of a speckle field, Phys. Rev. A **94**, 013835 (2016).

[26] H. E. Hernández-Figueroa, M. Zamboni-Rached, and E. Recami, *Non-Diffracting Waves* (John Wiley, New York, 2013).

[27] V. Arrizón, U. Ruiz, R. Carrada, and L. A. González, Pixelated phase computer holograms for the accurate encoding of scalar complex fields, J. Opt. Soc. Am. A **24**, 3500 (2007).

[28] A. Jesus-Silva, J. G. Silva, C. H. Monken, and E. Fonseca, Experimental cancellation of aberrations in intensity correlation in classical optics, Phys. Rev. A **97**, 013832 (2018).

[29] L. Mandel and E. Wolf, *Optical Coherence and Quantum Optics*, EBL-Schweitzer (Cambridge University Press, Cambridge, 1995).

[30] I. Vidal, D. P. Caetano, E. J. Fonseca, and J. M. Hickmann, Effects of pseudothermal light source's transverse size and coherence width in ghost-interference experiments, Opt. Lett. **34**, 1450 (2009).

[31] Y. Cai and S.-Y. Zhu, Ghost interference with partially coherent radiation, Opt. Lett. **29**, 2716 (2004).